Cell, Vol. 92, 547–557, February 20, 1998, Copyright ©1998 by Cell Press

Developmental Regulation of Vesicle Transport in *Drosophila* Embryos: Forces and Kinetics

Michael A. Welte,*§ Steven P. Gross,*†§ Marya Postner,* Steven M. Block,*† and Eric F. Wieschaus*‡
*Department of Molecular Biology
†Princeton Materials Institute
Howard Hughes Medical Institute
Princeton University
Princeton, New Jersey 08544

Summary

In *Drosophila* embryos, microtubules oriented along apical–basal directions support saltatory vesicle movement. Vesicle traffic includes lipid droplets whose distribution shifts twice during early embryogenesis. Using microscopy, optical tweezers, and a novel squashed-mount embryo preparation, we tracked single droplets and measured the forces these generated. Droplet stalling forces change developmentally, in a roughly quantized fashion, consistent with variation in the number of active motors. We characterized a mutation, *klarsicht*, that affects droplet transport. Klar$^+$ facilitates changes in force, possibly by coordinating the activity of multiple motors. Alterations in transport affected motion in both apical and basal directions, indicating tight coupling between motors of opposite polarity. Mutations in *klar* also affect nuclear migration during eye development, suggesting multiple roles for *klar*-based transport.

Introduction

Polarized cells face the problem of establishing an asymmetric distribution of their components. For small molecules or aggregates that travel short distances, purely diffusive motion suffices, but for larger objects and/or longer distances, active transport is required. Such transport relies on the action of motor proteins that move cargo along cytoskeletal tracks. Specific examples include the orchestrated movements of chromosomes during cell division (Hyman and Mitchison, 1991), the delivery of ribonucleoprotein particles in the developing oocyte of *Drosophila* (Wang and Hazelrigg, 1994), and the axonal transport of vesicles between nerve cell bodies and the synapse, in certain cases over distances of meters (Grafstein and Forman, 1980). Loss of transport machinery can lead to severe defects. In *Drosophila*, dynein is essential for cell viability (Gepner et al., 1996), while kinesin mutations disrupt axonal transport, leading to impaired function reminiscent of vertebrate motor neuron disease (Hurd and Saxton, 1996). A requirement for active transport is particularly evident in the development of early embryos, where an asymmetric distribution of components underlies the establishment of a basic body plan (e.g., Nüsslein-Volhard et al., 1987). Moreover, after fertilization, the cytoplasm is rapidly restructured on a massive scale (Foe and Alberts, 1983). These developmental rearrangements follow a stereotyped choreography, implying tight regulatory control. Understanding intracellular transport is thus not only a fundamental cell biological problem, but a key to development.

The basic machinery for transport has been identified: members of the dynein and kinesin superfamilies of motor proteins ferry a variety of cargoes along cytoskeletal microtubules (MTs). These cargoes include chromosomes, pigment granules, mitochondria, Golgi apparatus, and endosomes (Thaler and Haimo, 1996). However, exactly how the activity of motor proteins is integrated with the spatiotemporal control of transport remains unclear. Previous investigations have implicated phosphorylation of kinesin and dynein (or of associated protein complexes) in altering cargo specificity and/or motor activity (Sato-Yoshitake et al., 1992; Lee and Hollenbeck, 1995). Regulation of transport might conceivably be brought about in any of a variety of ways, for example: by changing the type or number of motors attached to vesicles, by altering the enzymatic activity of attached motors (thereby tuning the speed or force), or by adjusting the lengths of time during which motors continuously transport cargo unidirectionally before stopping or reversing.

To address regulation of transport, we studied saltatory vesicle motion in *Drosophila* embryos (Foe and Alberts, 1983). We chose to focus on the movement of storage organelles for neutral lipids, known as lipid droplets, which move in the periphery of embryos. This experimental system affords a number of advantages. *Drosophila* is amenable to genetic analysis, embryos at well-defined stages are easily selected, and we found stereotyped variations in vesicle traffic. Droplets are relatively large organelles ($\sim$0.5 μm diameter), which can be tracked at nanometer resolution by video-enhanced differential contrast interference (VE-DIC) microscopy coupled with computer-based centroid analysis. Moreover, highly refractive lipid droplets represent excellent candidates for manipulation by optical trapping ("optical tweezers"), permitting direct measurement of forces.

Using a combination of high-resolution optical tracking and ex vivo force measurements, we characterized the physical parameters associated with the transport of individual lipid droplets in *Drosophila* embryos. We were particularly interested in parameters that change at developmental transitions and thus might account for the bulk shifts in vesicle distribution. Our measurements of individual droplets are consistent with the observed bulk transport and suggest that understanding global motions can be reduced to unraveling the behavior of single vesicles. We also examined vesicle transport in embryos derived from mothers mutant for the *klarsicht* gene (Wieschaus and Nüsslein-Volhard, 1986). *klar* embryos show an altered distribution of lipid droplets at the onset of gastrulation and therefore are comparatively transparent. Historically, *klarsicht* (clear view) mutations have been introduced into fly stocks to produce photogenic

‡To whom correspondence should be addressed.
§These authors contributed equally to this work.

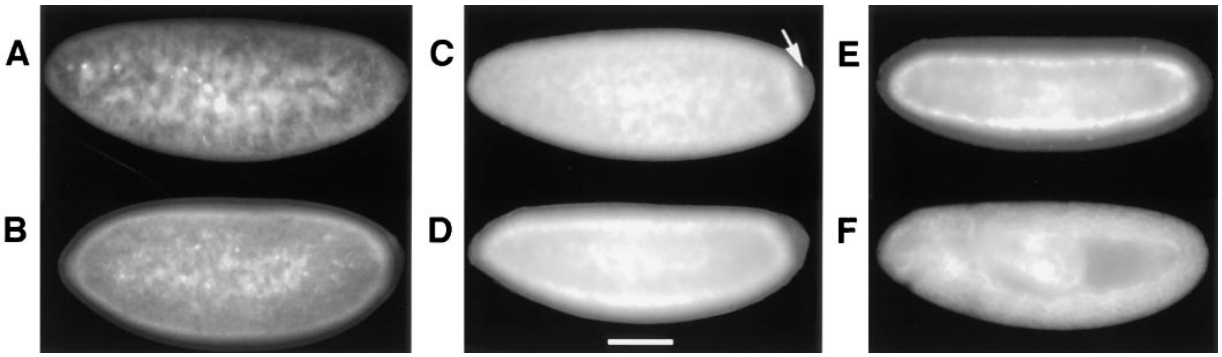

Figure 1. Bulk Movement of Kinesin–β-Galactosidase Fusion Protein and Lipid Droplets during Early Development

(A and B) Embryos expressing a kinesin–β-galactosidase fusion protein were fixed and stained to reveal its distribution. (A) Early syncytial blastoderm, showing a uniform distribution; (B) cycle 14, showing band of localization 35–40 μm from the surface.

(C–F) Embryos at different stages were stained with Nile Red to reveal the lipid droplet distribution. (C) Early syncytial blastoderm. Arrow, pole cells that are depleted of lipid droplets. (D) Before mitosis 13. Scale bar = 100 μm. (E) Midcellularization. (F) Germ-band extension.

embryos in which internal structures are more readily seen, but little is known about the *klar* gene and its function.

Results

The Distribution of Lipid Droplets Is Regulated

Several lines of evidence suggest that lipid droplets are transported by motors along microtubule (MT) tracks. First, during cycle 14, MTs extend radially inward, in basal–apical directions, coincident with droplet tracks (Fullilove and Jacobson, 1971). Second, a kinesin–β-galactosidase fusion protein that localizes to the plus ends of MTs in a variety of *Drosophila* cells (Giniger et al., 1993) is redistributed during the syncytial blastoderm stage, moving from an initially uniform distribution (Figure 1A) to a zone of high accumulation 35–40 μm below the surface (Figure 1B). This result confirms that MTs traverse the entire region over which saltatory transport has been observed (Foe and Alberts, 1983), with their plus ends located more centrally. Third, lipid droplet motion is first detected when cell nuclei (and associated centrosomes) reach the surface but ceases during syncytial mitoses, when cytoplasmic MTs are disassembled prior to the formation of spindles (Foe and Alberts, 1983; our unpublished data). Fourth, drugs that specifically destabilize MTs abolish saltatory movement of droplets almost immediately (Edgar et al., 1987). Finally, it seems unlikely that droplets could be driven by the polymerization or treadmilling of MTs, because polymerization rates (~20–30 μm/min in *Xenopus* egg extracts; Parsons and Salmon, 1997) are too slow to account for observed droplet speeds in excess of 1 μm/s.

The whole droplet population shifts dramatically during early embryogenesis. At the beginning of the blastoderm stage, droplets are found throughout the periphery (Figure 1C). Droplets visibly clear from the most peripheral zone after nuclei complete four additional rounds of division, and the embryo enters cycle 14 (Figure 1D). By the start of cellularization, most droplets are found in a band surrounding the central yolk (Figure 1E). Basal accumulation is reversed during the first 15 min of gastrulation, as droplets become redistributed throughout the cellular layer of the embryo (Figure 1F). Thus, the droplet population exhibits three distinct phases: phase I (syncytial blastoderm), corresponding to peripheral distribution (~45 min); phase II (beginning of cycle 14 until the end of cellularization), corresponding to basal accumulation (~55 min); and phase III (gastrulation), corresponding to apical redistribution (~20 min). Because lipid droplets are quite refractile and therefore scatter light, their movements generate global changes in the opacity of embryos. During phase II, yolk vesicles and lipid droplets draw back from the periphery, leaving in their wake a transparent zone ~35 μm deep (cytoplasmic clearing). By phase III, the embryo becomes opaque again as droplets shift apically (clouding).

We quantified redistribution during phase II by scoring the number of lipid droplets at various distances below the embryo surface by electron microscopy. In cycle 12 embryos, near the transition from phase I, droplets formed a broad, bell-shaped distribution, peaking between 18 and 30 μm beneath the surface (Figures 2A and 2E). For embryos in mid-phase II, when apical regions have been depleted of most of their lipid droplets, the region between 30 and 42 μm displayed a prominent peak (Figures 2B and 2F). At maximal clearing, by the end of cellularization at the transition to phase III, the distribution peak had shifted to the zone between 42 and 48 μm, with the majority of lipid droplets being found in the yolk sac, outside the newly formed cells (Figures 2C and 2G). The average distance of droplets from the surface increased roughly 10 μm during phase II. Because cell–yolk sac connections remain intact for some time thereafter (Rickoll, 1976), droplets remain free to move more apically during phase III. Although the total number of lipid droplets varied somewhat from embryo to embryo, we observed no systematic change in number with age, implying that redistributions occur via movements of existing droplets.

Lipid droplets cleared at nearly all distances from the periphery simultaneously but initially cleared more extensively from apical than from basal regions, resulting in transient increases of droplet populations in central compartments. These data exclude certain models of bulk droplet transport. Droplets are not carried basally

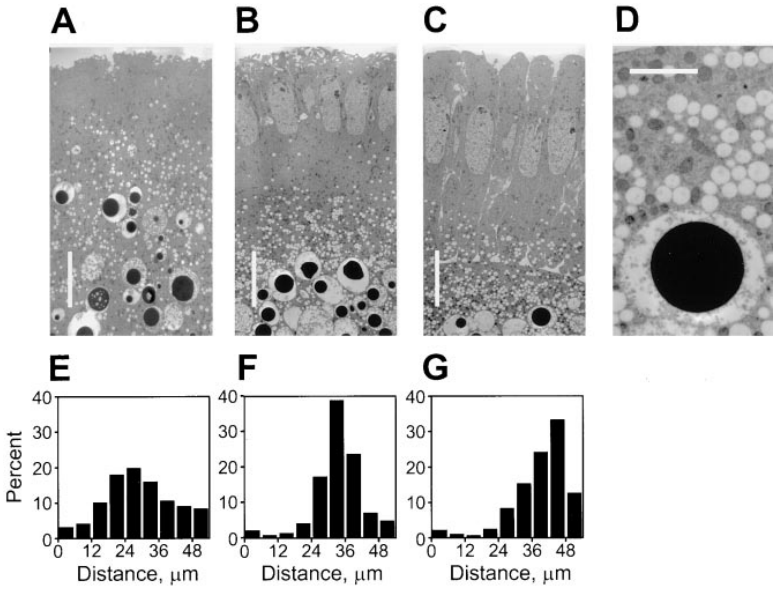

Figure 2. Clearing of Lipid Droplets from the Cortical Cytoplasm during Phase II

Electron micrographs of wild-type embryos from cycle 12 (A), cycle 14 early cellularization (B), and cycle 14 cellular blastoderm (C). Orientation: apical, top; basal, bottom (scale bar, 10 μm). Lipid droplets appear as small transparent circles. (D) A high magnification view (scale bar, 2.5 μm) shows one yolk vesicle (large sphere with dark inclusion), abundant lipid droplets (transparent spheres), and mitochondria (smaller, dark vesicles). (E–G) For each embryo, the graph below shows the percentage of droplets in various zones along the apical–basal axis.

by a bulk flow of cytoplasm, because in that case their spatial distribution would be expected to change little with time (and in any case, bulk flow cannot accommodate purely centripetal movement), nor are they swept inward by a moving sieve, for example, by a network of cytoskeletal fibers, because removal of droplets from apical regions would then precede transport in more basal zones.

Droplet Kinetics Explain Changes in Bulk Distributions

Is it possible to understand global transport from microscopic droplet behavior? To address this question, we developed a novel preparation to visualize and track individual lipid droplets at nanometer scale resolution. Single embryos at defined stages of development were dechorionated, placed on a glass microscope slide, and covered with halocarbon oil (Experimental Procedures). Embryos were then flattened between a cover glass and the slide, with the degree of compression being carefully controlled by spacers, to a final thickness of roughly 50 μm. This flattened preparation preserves the approximate geometry of the original embryo and supports vesicle motion up to 2 hr, ex vivo. The overall thinness of the preparation makes it well-suited for high numerical aperture (double oil immersion) optics, in combination with VE-DIC microscopy, affording the best possible spatial resolution during observations.

In general, droplets were selected for subsequent quantitative analysis from videotape recordings by eye; these tended to undergo sustained movement with considerable variation in speed (peak speed being several fold larger than average speed, up to roughly 1.5 μm/s in each direction). Because movements were both bidirectional and saltatory, records of individual droplets were first parsed into a series of segments representing more or less continuous motion in any one particular direction (Experimental Procedures). By analyzing images of droplet positions as functions of time, we extracted three statistics to characterize the microscopic motion: (1) the *persistence time*, the average amount of time spent during segments of travel exclusively in either the plus end (basal) or minus end (apical) direction, defined as $<t_+>$ or $<t_->$, respectively, (2) the *average distance* traveled during these segments in either direction, defined as $<d_+>$ and $<d_->$, and (3) the *average velocity* maintained during these segments, defined as $<v_+>$ and $<v_->$, and computed as a weighted mean (Table 1). Because few, if any, droplets remained stalled for significant periods of time, the population is characterized by the net difference between apical and basal segment motions. One can then derive a bulk displacement rate, *B*, which provides an estimate for the overall flux of droplets (Table 2). To illustrate, we compute *B* for the wild type in phase II. Subtracting the mean distance traveled by droplets moving apically, $<d_-> = 1092$ nm, from the mean distance traveled moving basally, $<d_+> = 1495$nm, yields a round trip distance of 403 nm. The average such round trip takes $<t_+> + <t_-> = 7.11$ s. Dividing the distance by time yields a bulk flux, *B*, of ~57 nm/s (3.4 μm/min) in the basal direction. The signs of fluxes computed from microscopic observations correctly predict the direction of all the fluxes observed: minimal shifts during phase I, net inward displacement during clearing, and net outward displacement during clouding.

Which microscopic parameters are modulated to cause the lipid droplet flux to change during the various phases? The difference between apical and basal accumulation is largely determined by the basal persistence time, $<t_+>$ (Table 1). In particular, the switch from basal transport in phase II to apical transport in phase III stemmed largely from the nearly 2-fold drop in $<t_+>$, while $<t_->$, $<v_+>$, and $<v_->$ remained almost constant.

klar Mutations Alter Statistics of Droplet Motion

Defects in vesicle movement potentially disrupt the normal sequence of clearing and clouding during development, resulting in abnormal distributions of the refractile lipid droplets. Mutations in organellar transport pathway

Table 1. Kinetic Parameters of Lipid Droplet Motion, Determined from Centroid Tracking of Individual Droplets

	Persistence Time, s Mean ± SEM (n)		Average Distance, nm Mean ± SEM (n)		Weighted Mean Velocity, nm/s Mean ± SEM (n)	
Embryo and Stage (n)	Basal, $<t_+>$	Apical, $<t_->$	Basal, $<d_+>$	Apical, $<d_->$	Basal, $<v_+>$	Apical, $<v_->$
wt phase I (3)	2.01 ± 0.09 (82)	2.16 ± 0.13 (79)	1073 ± 164 (82)	1219 ± 188 (79)	407 ± 49 (82)	475 ± 42 (79)
wt phase II (2)	4.46 ± 0.12 (61)	2.65 ± 0.47 (57)	1495 ± 41 (61)	1092 ± 143 (57)	321 ± 15 (61)	359 ± 50 (57)
wt phase III (2)	2.50 ± 0.35 (54)	2.76 ± 0.11 (53)	815 ± 25 (54)	1140 ± 52 (53)	285 ± 66 (54)	378 ± 35 (53)
klar phase II (3)	2.7 ± 0.26 (107)	1.93 ± 0.21 (108)	547 ± 95 (107)	413 ± 25 (108)	162 ± 40 (71)	134 ± 12 (79)
klar phase III (3)	3.45 ± 0.15 (124)	2.59 ± 0.60 (116)	871 ± 148 (124)	593 ± 97 (116)	210 ± 30 (124)	191 ± 24 (116)

genes might therefore be recognized by altered opacity in affected embryos. *klar* is one such mutant (Wieschaus and Nüsslein-Volhard, 1986): *klar* embryos are more transparent, but the underlying cellular defect has not been characterized.

The *klar* phenotype is most apparent during phase III of transport. Embryos laid by females homozygous for presumptive null alleles of *klar* (termed "*klar* embryos", here) are unusually transparent from gastrulation onward (Figures 3A and 3B). The lipid droplets of such embryos were concentrated in the yolk sac (Figure 3D), rather than distributed throughout the cellular layer, as in wild type (Figure 3C), because during gastrulation, basally accumulated droplets spread apically to only a minor degree (data not shown). During phase II, *klar* embryos were indistinguishable from wild type, as judged by video analysis of living embryos (Figures 3E and 3F), lipid droplet staining (Figures 3G and 3H), and electron microscopy (Figures 3I, 3J, 3K, and 3L).

However, higher resolution video recordings from intact *klar* embryos, as well as measurements in flattened preparations, revealed a severe impairment of motion: during all three phases, droplets moved less frequently and less vigorously than in wild type. This difference is particularly evident in phase II, where the basal and apical velocities and travel distances are less than half that of the wild type (Table 1). In both phases, $<t_+>$ is significantly larger than $<t_->$, tilting the balance toward a net basal flux, which prevents reclouding in mutant embryos.

klar mutations affect lipid droplet transport, but video and electron microscopic analysis revealed no defects in cellularization and gastrulation or altered distributions of embryonic nuclei, yolk vesicles, or mitochondria. In particular, during phase II the kinesin–β-galactosidase fusion protein accumulated basally, just as in wild type (data not shown), indicating that the polarity of MT tracks was undisturbed. Although eye development is disrupted (see below), mutant embryos nevertheless develop into viable, fertile adults.

Forces Driving Lipid Droplets Are Developmentally Controlled

To investigate the physical mechanism responsible for altered droplet motion in *klar* embryos, we used optical tweezers to measure the forces powering droplets. Infrared laser-based optical traps (optical tweezers) can be used to manipulate and exert controlled forces on small, refractile particles (Svoboda and Block, 1994a; Visscher et al., 1996). By attaching kinesin proteins to uniform microscopic beads, optical tweezers have been used to measure the elementary steps and forces produced by single motors moving along MTs in vitro (Svoboda et al., 1993; Svoboda and Block, 1994b). Optical tweezers can also be used to exert forces on refractile organelles inside living cells (Ashkin et al., 1990). We have adapted this approach to quantitate the forces powering lipid droplet transport in preparations of flattened *Drosophila* embryos. Calibrations were accomplished using a variation of the "escape force method" (Figure 4A; Experimental Procedures). At a given laser power, only a fraction of droplets are stopped: those that escape are pulled by motors exerting forces greater than those applied by the trap. For each developmental phase and genotype studied, the fraction of lipid droplets escaping from the trap was scored as a function of laser power. Beyond some critical laser power, F_c, all droplets become stalled. The relationship between laser power and the proportion of organelles escaping the trap was used to estimate the mean stall force, F_{st}, for lipid droplet motion (Experimental Procedures).

In wild-type embryos, the mean droplet stall force varied markedly with the developmental stage (Figures 4B and 4C). From 3.3 pN during phase I, F_{st} increased to 5.5 pN in phase II, then returned to an intermediate level of 4.7 pN during phase III. Despite this developmental variation, the forces were nearly the same for droplets escaping in either the apical or basal directions. At any given laser power, the percentage of droplets stalled in either direction was the same to within the standard error of the measurement, typically about 5% (data not shown). The *klar* mutation, in contrast, generated comparatively low stall forces, 1.2 pN, that were independent of the direction of movement and did not change with the developmental stage.

Table 2. Predicted Droplet Fluxes, *B*, Calculated from the Kinetic Parameters of Table 1

	Predicted Bulk Displacement, *B* Mean ± SEM	
Embryo and Stage (n)	Direction	Rate (μm/min)
wt phase I (3)	(none)	2.1 ± 4.9
wt phase II (2)	basal	3.4 ± 1.5
wt phase III (2)	apical	3.7 ± 0.9
klar phase II (3)	basal	1.7 ± 1.0
klar phase III (3)	basal	2.7 ± 2.4

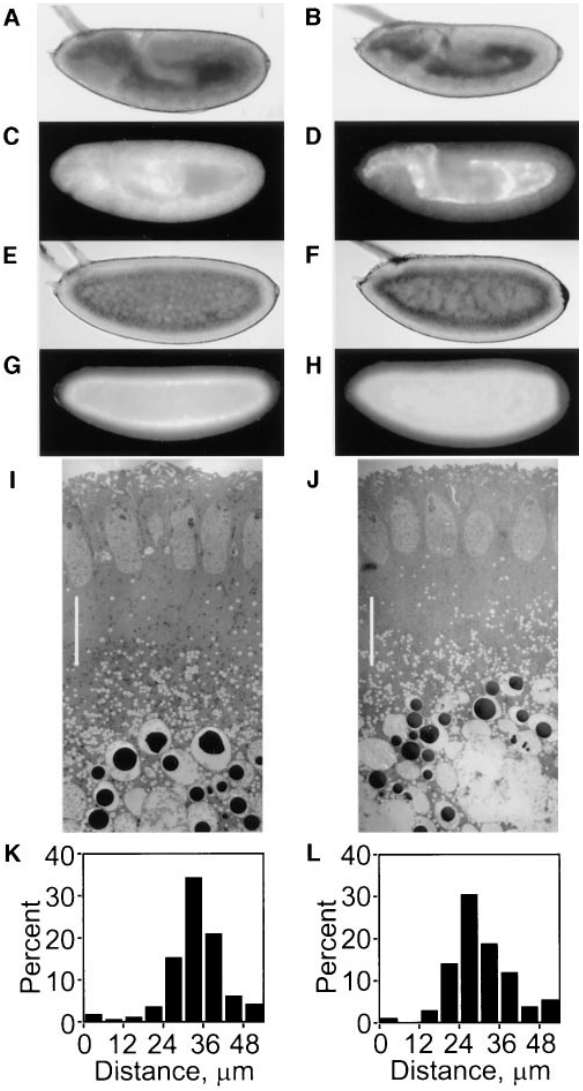

Figure 3. *klar* Alters Global Droplet Distribution in Phase III, but Not in Phase II

Wild-type (left panels) and *klar* (right panels) embryos were compared while alive (A, B, E, and F) or after fixation and staining with Nile Red (C, D, G, and H) as in Figure 1, or by electron microscopy (I–L) as in Figure 2 (scale bar, 10 μm). After clouding stages (germband extension, A–D), *klar* embryos are more transparent due to basally accumulated lipid droplets. In phase II (early cycle 14, E–L), *klar* embryos are indistinguishable from wild type.

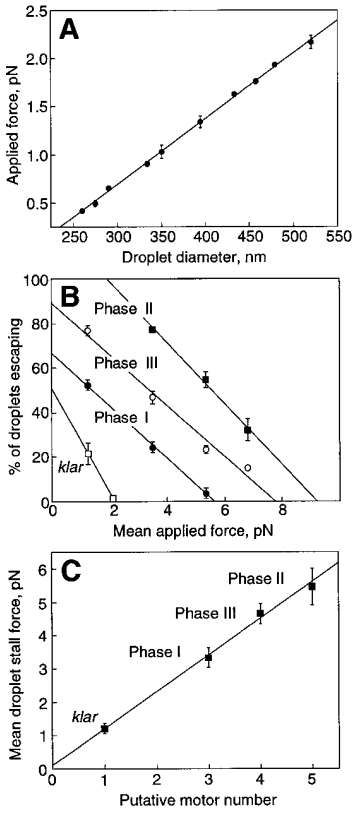

Figure 4. Stall Forces Change throughout Development

(A) Calibration. Droplet diameter versus escape force from the optical trap. Each point represents an average of four lipid droplets of similar size; the data are fit to a linear relationship (solid line).

(B) Embryo stall force measurements. Percentage of droplets escaping the optical trap as a function of a variable trapping force, achieved by adjusting the laser power. Data points summarize measurements from 5–10 embryos, with 30–50 droplets tracked per embryo. The x-intercept for each fit line represents the extrapolated critical force, F_c, beyond which no droplets escape.

(C) Mean droplet stall force, F_s, plotted against the presumed number of active motors. F_s values were computed from the F_c determinations in (B) by applying corrections, as described in the Experimental Procedures. The slope of the weighted line fit (solid line) corresponds to 1.10 ± 0.04 pN/motor; note that the unconstrained fit passes nearly through the origin (y-intercept 0.10 ± 0.09 pN).

Plus and Minus End Motion May Rely on Different Motors

Kinesin molecules move along linear tracks parallel to individual protofilaments of the MT lattice (Gelles et al., 1988; Ray et al., 1993). As a consequence, beads driven toward the plus ends of MTs by single kinesin motors in vitro display remarkably little side-to-side motion (Gelles et al., 1988). Conversely, beads driven by cytoplasmic dynein molecules wander freely over the MT surface lattice while proceeding toward the minus end, resulting in a substantially greater lateral motion (Wang et al., 1995). We monitored the mean lateral displacements for the droplets in our preparations. In wild-type embryos, lateral displacements were consistently larger when droplets moved apically, toward the minus ends of MTs (Table 3). In *klar* embryos, however, the lateral displacement was the same for both directions of travel.

Table 3. Average Lateral Displacements of Droplets Moving Apically or Basally

	Lateral Displacement, nm Mean ± SEM (n)	
Embryo and Stage (n)	Basal Travel	Apical Travel
wt phase I (3)	31.3 ± 2.2 (54)	49.7 ± 9.0 (50)
wt phase II (2)	32.6 ± 2.5 (53)	43.5 ± 5.0 (35)
wt phase III (2)	37.6 ± 2.9 (56)	52.7 ± 5.7 (50)
klar phase II (2)	26.3 ± 2.0 (58)	27.7 ± 2.1 (49)
klar phase III (3)	25.9 ± 1.9 (56)	30.3 ± 2.5 (42)

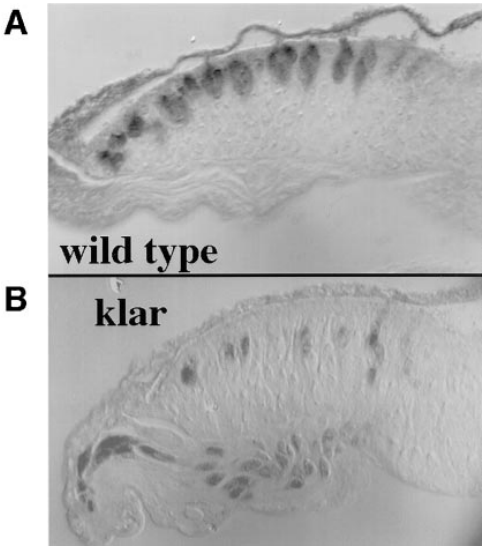

Figure 5. *klar* Causes Mislocalization of Photoreceptor Nuclei in Developing Eye Discs

Eye imaginal discs from wild-type (A) and *klar* (B) third-instar larvae were fixed, stained for the neural antigen Elav, and sectioned longitudinally. (Orientation: apical, top; basal, bottom; anterior, right; posterior, left.) The optical stalk extends from the epithelium basally and posteriorly.

klar Mutations Disrupt Nuclear Migration

As well as impairing lipid droplet motion, *klar* mutations disturb eye development. In third-instar eye discs, staining for the nuclear antigen Elav showed that photoreceptor nuclei were mispositioned along the apical–basal axis. In the wild type, nuclei are normally positioned in clusters near the apical surface of the eye disc (Figure 5A), whereas in *klar*, few such nuclei remained in apical regions. Instead, most nuclei were found near the basal surface, and a number had even migrated into axons of the optic stalk (Figure 5B). In cross sections of adult *klar* eyes, the rhabdomeres of many photoreceptor cells were either misshapen or missing altogether (data not shown). Mutations in the *marbles* gene (*marb*) cause a similar mislocalization of nuclei and also produce misshapen rhabdomeres (Fischer-Vize and Mosley, 1994). Deletion analysis mapped *klar* close to *marb*, and all *marb* alleles we examined ($marb^{CD4}$, $marb^{BX3}$, and $marb^{BP3}$) had additional defects in lipid droplet transport. Furthermore, *klar* and *marb* alleles failed to complement one another, both for the adult eye and droplet transport defects (*data not shown*). We conclude that *marb* and *klar* represent the same gene.

Discussion

In vivo organelle transport has previously been investigated in a variety of systems where vesicle motion persists for minutes to hours (Brady et al., 1985; Schliwa et al., 1991; Thaler and Haimo, 1992; Hamm-Alvarez et al., 1993). Our ex vivo approach continues in this tradition but allows genetic analysis as well. Additionally, the stereotyped changes in transport that occur during development allow one to study concomitant changes in motor properties.

Working in semiintact preparations entails certain limitations. For example, there are larger uncertainties in force and position than for work in vitro, and the molecular components are numerous and largely undefined. In particular, we do not yet know which molecular motors power lipid droplets. However, because genetic and molecular analysis is well-developed in *Drosophila*, it should be possible in the future to characterize the components of this transport system, for example, by investigating the effects of mutations in MT motor proteins (Saxton et al., 1991; Gepner et al., 1996).

One particular strength of this system is that we can link local and global aspects of transport. Is the bulk flux inferred from microscopic observations sufficient to account for the change in global droplet distribution? The periphery of phase II embryos clears within 40 min, with the major decrease in opacity occurring in just 10 min. The droplet population as a whole shifts basally through roughly 10 μm during phase II, yielding an average transport rate of 0.25–1 μm/min. Certain subpopulations have higher rates because the extent of bulk transport varies with time and position along the apical–basal axis; for example, initially droplets clear more extensively from apical than from basal regions. The calculated flux rate of 3.4 μm/min for phase II is more than sufficient to accommodate this global redistribution and suggests that factors other than the mobility of individual droplets may limit bulk transport, for example: the rate with which MTs regrow after mitosis 13, the slowing of transport as lipid droplets pile up basally, or the interference from yolk vesicles that accumulate to high densities in the basal-most region.

The calculated bulk flow is also of sufficient magnitude and appropriate direction to account for droplet population shifts in all other stages examined. In wild-type phase III embryos, apical fluxes are consistent with clouding behavior; in *klar* phase III embryos, basal flux prevents this clouding.

Forces In Vivo

Our measurements permit quantitation of changing motor forces during development. Mean stall forces appeared to be quantized in discrete multiples of about 1.1 pN (Figure 4C). What could be the basis for this phenomenon? Assuming that the applied load were distributed equally among multiple motors, and that these acted independently, one would expect the stall force for two motors to be double that of a single motor, subject to simplifying assumptions about the motor duty cycle, discussed below (see Model). In support of this, preliminary experiments with silica beads carrying limiting amounts of squid kinesin protein moving on microtubules in vitro suggest that the stall force for two kinesin molecules is indeed double that of one (S. M. B., K. Visscher, and M. J. Schnitzer, unpublished data). Consistent with this picture, *klar* droplets, with a stall force near 1.2 pN, could carry one active motor ($<n> = 1$); phase I droplets, three active motors ($<n> = 3$); phase III droplets, four active motors ($<n> = 4$); and phase II droplets, five active motors ($<n> = 5$). Empirically, there

is a linear relationship between stall forces and presumed motor number, with the unconstrained line fit passing through the origin (Figure 4C).

The "unit motor" producing a unitary force of 1.1 pN could, of course, represent either a single motor molecule or a complex of several motors acting in concert. A unitary force of 1.1 pN seems somewhat low compared to the 4–6 pN measured for squid kinesin in vitro (Svoboda and Block, 1994b). Lipid droplet motors may be less powerful, or active motors may display different behaviors in vivo and in vitro. An earlier force measurement of vesicle movement in *Reticulomyxa* also reported lower values than those found for kinesin (~2.6 pN per motor, but with an uncertainty of a factor of 2–3; Ashkin et al., 1990).

Persistence Control

Lipid droplets appeared to be in constant motion, remaining stationary for negligible times. Their bulk transport could be regulated, in principle, either by changing the droplet velocity or droplet persistence time, in either or both directions. In wild-type embryos, the largest difference in bulk transport was observed between phases II and III, when droplet velocities remained unchanged. Instead, changes in droplet flux seemed to be governed mainly by changes in the persistence time, specifically that of droplets moving basally. To control the persistence time, either the number of motors or the enzymatic activity of individual motors could be altered. Attaching multiple motors to droplets would have the effect of increasing the persistence time by raising the probability that at least one motor remained bound. The basal persistence measured in the wild type is consistent with this proposal, assuming that changes in force do indeed result from changes in motor number: the persistence time is longest in phase II (five motors), shorter in phase III (four motors), and shortest in phase I (three motors). However, this correlation is not observed in *klar* embryos or in apically directed movement in wild-type embryos. Thus, changes in force and presumed motor number cannot be the only factors affecting the persistence time.

Coupling of Motion in Opposite Directions

Several lines of evidence suggest some form of coupling between apical and basal motion. First, the apical and basal unitary forces are of equal magnitude. Second, apical and basal stall forces tend to change together, preserving a rough balance of forces. Third, in *klar* embryos, stall forces are reduced in both directions. Such tight coupling could result if both basal and apical transport relied on a single, bidirectional motor. A bidirectional motor has been proposed for *Reticulomyxa*, where a dynein-type complex is thought to be responsible for fast (~9.5 μm/s) transport of organelles in both the anterograde and retrograde directions. The alternate possibility is that entirely different motors subserve the motions in either direction but that these motors are coordinately controlled and have similar properties.

The change in lateral displacement of wild-type droplets when moving in opposite directions suggests a change in the physical interaction between the droplet and MT correlated with polarity. The simplest explanation for this difference is that there are distinct plus and minus end–directed motors, which either differ in size, affecting the length of the linkage between the MT and droplet, or differ in the ways in which they proceed along the MT surface lattice. A bidirectional motor cannot be ruled out, however, provided that its properties changed sufficiently with directional polarity. For now, the leading candidate for the apical (minus end–directed) motor is a cytoplasmic dynein, primarily because this is the only minus end–directed motor known to generate velocities up to 1.5 μm/s, similar to those observed. Moreover, the increase in lateral displacement observed during apical motion is roughly comparable to that measured for cytoplasmic dynein in vitro, which wanders over the MT surface lattice (Wang et al., 1995), in contrast with native kinesin, which tracks strictly along single MT protofilaments (Gelles et al., 1988; Ray et al., 1993) (Experimental Procedures). Both the velocity and the reduced lateral displacement associated with basal motion are consistent with a kinesin or kinesin-related protein (Gelles et al., 1988; Wang et al., 1995).

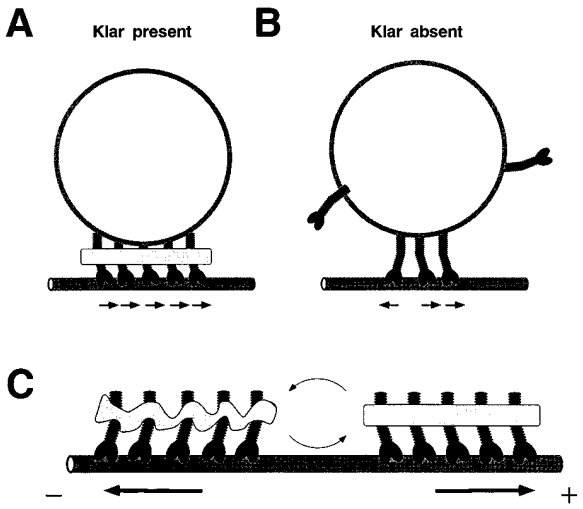

Figure 6. Features of the Klar$^+$-Dependent Transport System

(A) Klar$^+$ coordinates multiple motors on a lipid droplet. (B) Absence of Klar$^+$ results in a tug-of-war. (C) Klar$^+$ coordinates multiple motors so that they switch direction simultaneously. This cartoon is based on a single species of bidirectional motor, but analogous models are possible for distinct plus and minus end–directed motors.

Model

One of the challenges of employing multiple motors is their coordination. If motors had a short duty cycle, producing force during only a tiny fraction of the time they are moving on MTs, it would be necessary to have some means of synchronizing their activity in order for their individual forces to summate. To avoid a tug-of-war situation, motors of opposite polarities may not remain continually bound and active on the surfaces of vesicles. We hypothesize that the Klar protein solves these kinds of problems in the wild type by establishing a tightly coordinated complex of motors (Figure 6A).

Several lines of evidence suggest that coordination

breaks down in the absence of Klar (Figure 6B). The difference in lateral displacement between motions in the apical and basal directions disappears in *klar* embryos. Next, the anticipated competition between motors of opposite polarities in *klar* embryos might be expected to affect both velocity and force deleteriously. Consistent with this, we observed a reduction of velocity for droplets in *klar* embryos to about half that of the wild type. This change is similar to the reduction in the velocity of gliding microtubules moving in vitro in a competition assay using both dynein and kinesin, reported by Vale and coworkers (Vale et al., 1992). Moreover, lipid droplets in *klar* embryos are readily stalled by forces of a magnitude close to the unitary force (Figure 4C). This suggests that droplets are either (1) propelled by a single motorcomplex or (2) propelled by multiple motors of both polarities, but with a number excess of just one, on average, pulling in any given direction.

Our model, then, is one where $Klar^+$ enforces the coordination of same-direction motors and thus avoids a tug-of-war, by switching off the plus end–directed motors when minus end–directed motors are active, and vice versa. We postulate that the $Klar^+$ complex either alternates the presentation of plus end–directed or minus end–directed motors to the MT, or that it couples several bidirectional motors, such that they switch directions synchronously (Figure 6C). Regulation of this complex alters the frequency of switching, affecting persistence times and thus determining the direction of net transport. At the same time, the complex also controls the number of actively engaged motors.

This model makes testable predictions. First, the Klar protein should be found on lipid droplets and potentially in direct association with motors. Second, multiple motors should be found on droplets. Third, the motor–Klar complex should be subject to regulation that directly affects its physical properties.

klar Mutations Reveal a General Transport System

As photoreceptor cells mature, their nuclei are transported over tens of microns, first in the basal and then in the apical direction (Tomlinson, 1985), reminiscent of lipid droplet transport in phase II and III embryos, respectively. *klar* mutations disrupt both transport processes similarly, impairing the ability to switch from basal to apical transport. This parallel suggests the existence of a general system for bidirectional transport of organelles, including embryonic lipid droplets, photoreceptor nuclei, and possibly other cargoes. At least in the eye disc, this transport system appears to rely on dynein, because a dominant mutation in $p150^{Glued}$ (a subunit of dynactin, the dynein activating complex) causes basal mislocalization of photoreceptor nuclei that is strikingly similar to that of *klar* mutants (Fan and Ready, 1997).

How similar is the role of Klar in the transport of lipid droplets and nuclei? In fungi, two contrasting mechanisms have been proposed for nuclear migration (Morris et al., 1995). In one view, nuclei are uncoupled from any microtubule organizing center (MTOC) and are propelled along MTs by cytoplasmic dynein directly, just as any cargo. In the other, nuclei are fastened to the MT network through an MTOC, and dynein anchored in the cytoplasmic membrane reels in the nuclei by translocating the MTs, also promoting their depolymerization in the process. If the first mechanism operates in photoreceptor cells, nuclei could employ the same Klar-based multimotor complexes that we postulate for lipid droplets. In the second case, Klar may organize individual dyneins at the apical membrane into efficient multimotor machines, in whose absence too little force is generated to pull nuclei apically. Because these two mechanisms predict different locations of motors and MT ends relative to the nucleus (Morris et al., 1995), they may be distinguishable by determining the intracellular location of dynein and the polarity of MTs, for example, with kinesin fusion proteins (Giniger et al., 1993).

In summary, the *klar* and wild-type phenotypes reveal a general, microtubule motor-based system, which regulates switching between different directions of transport. Using the tools introduced here to visualize and quantitate lipid droplet movement in embryo preparations, it should be possible to eventually dissect many of the physical properties of this general system. Of particular interest will be mechanisms of developmental regulation and the coordination of multiple motors, issues not readily addressed using simpler in vitro motility assays.

Experimental Procedures

Fly Stocks

Oregon-R was the wild-type stock. By deficiency analysis, *klar* maps to chromosome region 61C (unpublished data), close to *marb* (61C4–7). All of the quantitative analysis reported here employed the original $klar^1$ allele. $klar^1$ and four newly identified *klar* alleles (unpublished data) caused similarly transparent embryos and rough eyes, in various allele combinations and over a deficiency ($Df(3L)emc^{E12}$; Garcia-Alonso and Garcia-Bellido, 1988) that removes the *klar* locus. This suggests that $klar^1$ is a null allele. All known *klar* and *marb* alleles are viable and fertile. To establish how far MTs extended into embryos, we employed line KZ328 (Giniger et al., 1993), which expresses a kinesin–β-galactosidase fusion protein in early embryogenesis.

Visualizing Kinesin–β-Galactosidase, Photoreceptor Cell Nuclei, and Lipid Droplets

The kinesin–β-galactosidase fusion protein was detected as described by Giniger et al. (1993). Eye imaginal discs were fixed, stained for Elav, and sectioned essentially as described by Fischer-Vize and Mosley (1994). To label lipid droplets, dechorionated embryos were fixed for 1 hr in a mixture of PBS, formaldehyde, and heptane (1:1:2), dried briefly, stained with 0.8 μg/ml Nile Red (Sigma) in PBS, counter-stained with Hoechst 33258 (to label nuclei), mounted in 75% glycerol, and scored by epifluorescence microscopy. Nile Red specifically labels lipid droplets in cultured mammalian cells (Greenspan et al., 1985); and in *Drosophila* embryos, Nile Red staining correlates with the distribution of lipid droplets as determined by electron microscopy. Oil Red O (Preece, 1972), a dye specific for neutral lipids, produces a virtually identical staining pattern (data not shown).

To confirm the identity of moving particles seen by light microscopy, we suspended dechorionated, gastrulating embryos in drops of PBS and gently squashed these to disperse the cells. In a subset of such cells, large particles continued to move in a saltatory fashion on linear paths at speeds comparable to vesicular movement in intact embryos. These moving particles were ~0.5 μm in diameter and labeled strongly with Nile Red.

Electron Microscopy

Syncytial blastoderm and cellularizing embryos were collected, fixed, stained, embedded for electron microscopy, and sectioned as described by Merrill et al. (1988). For each embryo, we determined the number of lipid droplets along the apical–basal axis, in zones 6 μm wide, averaged over at least seven nonoverlapping sections, and from these data calculated the mean distance of droplets from the surface. To determine the degree of variation, we analyzed two or more embryos of each stage.

Droplet Motion in Intact Embryos and Squash Preparations

Intact, mechanically dechorionated embryos were placed on Petriperm plates, covered with halocarbon oil plus a cover glass, and lipid droplet motion was recorded on a time-lapse video recorder (AG-6030, Panasonic) using differential interference contrast (DIC) microscopy on an upright microscope (Axioplan, Zeiss). Tracks of individual droplets that could be readily visualized were traced on a video screen and measured; such droplets moved apically at speeds from 0.8 to 1.5 μm/s (average 0.77 μm/s; n = 13) and basally at speeds from 0.3 to 0.6 μm/s (average 0.45 μm/s; n = 16). Frequency and extent of travel diminished during syncytial mitoses, with an especially pronounced pause at the end of cycle 13 (Foe and Alberts, 1983).

For higher resolution work, single embryos of well-defined stages were chosen: for phase I, embryos came from mitotic cycles 10, 11, or 12; for phase II, embryos came from early cycle 14, where cellularizing membranes had not advanced beyond more than half the extent of the nuclei; and for phase III, embryos had initiated gastrulation. Dechorionated embryos were placed on a microscope slide and covered with halocarbon oil. A cover glass was placed gently on top of this preparation, supported by two spacers on either side, which served as props. On one side, the spacer consisted of a second cover glass ~160 μm thick. On the other, it consisted of a single layer of double-sticky tape (3M, Inc.), ~80 μm thick. After the thicker spacer was removed, surface tension pulled down on the cover glass, gently squeezing the embryo, such that its yolk was partially extruded and structures that normally extend radially became closely apposed to the cover glass surface. Frequently, regions of such squashed preparations preserved much of the cellular morphology and maintained active areas of saltatory motion of lipid droplets, in planes parallel to the coverslip. Vigorous motion was reproducibly observed for tens of minutes, and in some instances forces appeared undiminished for periods of up to 2 hr. For kinetic and force analysis, we restricted our measurements to the first 15–30 min after squashing. During this time, preparations seemed to faithfully recapitulate movements in the intact embryo; in both, motion occurred in the same directions and with similar velocities.

Video Analysis

Droplet motion was visualized by video-enhanced DIC microscopy (Axiovert 100, 100X/1.3NA oil immersion objective, 1.4 NA oil condenser, Zeiss; C2400 CCD video camera; Argus-20 image processor, Hamamatsu) and videorecorded (AG-6300, Panasonic). Motion sequences, 10–15 s in duration, were transferred from videotape to an optical memory disk recorder (TQ2028-F). The positions of individual droplets were tracked frame by frame using an algorithm that calculates the position of the image centroid by cross-correlation and that is accurate to the subpixel level (Image-1, Universal Imaging; see Gelles et al., 1988). This procedure provides centroid coordinates with a temporal resolution of 33 ms and a spatial resolution of ~5 nm. The standard deviation in position of a nonmoving droplet stuck to the coverslip was ~2 nm.

Centroid-based trajectories of moving particles were decomposed into two separate motions, parallel and perpendicular to the major axis of displacement (Gelles et al., 1988), using a program incorporating a least squares line fit algorithm, which minimizes the net perpendicular distance of the experimental data to the fit line (S. M. B., unpublished data). Records of motion in the parallel direction were used to extract the kinetic data; records of motion in the perpendicular direction were used to estimate the lateral displacement (see below). This procedure assumes that objects moved along straight average paths throughout the region tracked. To deal with the issue of saltatory movement, parallel records were parsed into alternating segments of plus or minus end–directed motion, based on "reversal points": those times at which droplets reversed direction, thereafter traveling a minimum of 100 nm in the opposite direction. At any given time, fewer than 5% of droplets were found to be "stalled" (operationally defined as having a mean velocity below 60 nm/s for more than 0.5 s), and such droplets typically remained stalled for under 2 s. Droplet movement was therefore modeled as a two-state (i.e., binary) system, consisting of purely plus or minus end–directed motion. The distance and duration for each segment were measured, and the average droplet velocity in a segment was computed from the ratio. Pooled data from all run segments in a given direction, derived from a series of tracked droplets, were used to compute mean distances, $<d_+>$ and $<d_->$, and mean persistence times, $<t_+>$ and $<t_->$. Mean velocities, $<v_+>$ and $<v_->$, were computed from weighted averages of speeds for all segments, with individual segment weights being assigned based on the propagation of errors in time and distance for each segment (Bevington, 1969).

We computed lateral displacement from the standard deviation of perpendicular displacement data, derived from lines fit locally to relatively short, representative segments of runs in a single direction (typically, 5 μm), rather than to the line fit of an entire droplet track. This procedure was adopted to insure that small amounts of curvature present in the overall trajectory track did not introduce systematic offsets. The method may underestimate the lateral displacement when used on short segments, as the mean droplet position may not accurately reflect the location of the MT axis.

Optical Trapping

The optical trap used for this work was produced by an 840 nm, single mode diode laser with integral beam circularization optics (200 mW, Melles Griot; Visscher et al., 1996). Trapping light levels were controlled with a dual-wedge compensating attenuator (925B, Newport). Droplets were trapped within 10 μm of the cover glass surface. Trapping force was calibrated by the escape force method (below; see also Visscher et al., 1996) and varied linearly with droplet size over the range studied (Figure 4A). Droplet diameter was found to be distributed in Gaussian fashion (0.46 ± 0.09 μm; mean ± standard deviation, n = 150). This distribution appeared to be the same in all embryos, mutant and wild-type, throughout the developmental phases studied. Droplet size was determined by applying small corrections to the apparent image size of droplets seen in video using a calibration curve. This curve was constructed by measuring the image sizes of silica beads of known diameters over the range 0.3–1.0 μm (index of refraction, n= 1.47). The refractive index for silica is comparable to that of lipid droplets (n = 1.48–1.53; Tiffany, 1986; White et al., 1996).

Force Calibration

The escape force from the optical trap was found for 0.5 μm uniform silica beads (gifts of Egon Matijevic) in a variety of sucrose solutions with concentrations ranging from 0%–40% w/v (index of refraction n = 1.33–1.40; Weast, 1986). Multiple determinations of escape speeds (averaged from video records of trials where the microscope stage was manually accelerated until particles just escaped from the trap) were converted to force using the known viscous drag, computed from the bead diameter and solution viscosity (Weast, 1986; Visscher et al., 1996). There appeared to be little change in trapping efficiency over this range of refractive indices: the escape force remained nearly constant, to within 10%. Trapping forces are expected to be comparable in vivo, since the refractive index of cytoplasm typically falls in the range of n = 1.37–1.40 (Bereiter-Hahn et al., 1979; Valkenburg and Woldringh, 1984). Escape forces in vivo were therefore calibrated using the viscous drag method in motility buffer (Visscher et al., 1996), using purified lipid droplets of different known size (Figure 4A). To retrieve lipid droplets for calibration, 3-to-5-hr-old embryos were homogenized in phosphate-buffered saline (containing protease inhibitors: 2 μg/ml Aprotinin, 0.5 mg/ml AEBSF, 1 μg/ml pepstatin A, 1 μg/ml leupeptin, 0.5 mg/ml TAME) and centrifuged at low speed to remove large particles (microfuge, 4K for 10 min). The supernatant was recentrifuged at

high speed (microfuge 14k, 10 min), and the lipid-rich top layer was recovered. This layer is greatly enriched for lipid droplets, as judged by Nile Red staining and the size of the recovered vesicles. This preparation was diluted in motility buffer (80 mM PIPES, 1 mM EGTA, 4 mM $MgCl_2$ [pH 6.9]).

In Vivo Measurements

In flattened embryos, individual lipid droplets moving along MTs were trapped, and the fraction escaping the trap at a given laser power was scored. Where possible, the laser power was then slowly increased until eventually all trapped droplets were stalled by the trap (Figure 4B). This proved to be feasible in *klar* mutant embryos and for the wild type during phase I. In the wild type in phases II and III, where forces were higher, the laser power was raised instead to its maximal level (~200 mW) and an extrapolation was performed (see below). From the relationship between the fraction of droplets escaping and the light level, an estimate of the mean population stall force, F_{st}, was derived as follows.

Because of the nearly linear relationship between droplet size and force (Figure 4A), a Gaussian distribution in droplet sizes yields a Gaussian distribution of applied optical forces, with $\sigma_f = k\sigma_d$, where σ_f is the standard deviation in force, σ_d is the standard deviation in droplet size (equal to 0.09 μm, above), and k is the slope of the force diameter calibration curve for the appropriate laser power, an example of which is shown in Figure 4A. At an intermediate laser power, the optical forces on statistically smaller droplets will be lower, and therefore some variable fraction of these will escape when propelled by a given motor force. The minimal laser power required to trap nearly all the droplets in a preparation represents a critical force, which operationally (and somewhat arbitrarily) we took to represent a force, F_c, of a magnitude two standard deviations ($2\sigma_f$) greater than the mean. The escape force corresponding to a mean-sized droplet, F_{st}, was therefore calculated from F_c by applying the correction $F_{st} = (F_c - 2\sigma_f) = (F_c - 2k\sigma_d)$. Values for F_c were obtained from the x-intercepts of lines fit to the data in Figure 4B, that is, to the apparent force beyond which no droplets should escape, and adjusted by $2k\sigma_d$, which ranged from 0.84 (*klar*) to 3.78 pN (phase II). This extrapolation procedure was adopted to accommodate the experimental data in a fairly even-handed manner. In principle, the relationship between the fraction of droplets escaping and the motor force should be described by an error function (the integral of a Gaussian distribution), rather than by straight lines, if the only source of system variance were droplet size. Empirically, however, the variation in escape force is broader, by roughly a factor of 2, than that predicted by the variance in droplet size alone. This, we assume, is due to additional contributions, such as variance in the motor number and/or variance in the single motor force.

Over the few seconds required to stall a droplet, laser-induced photo damage did not seem to be a problem: stalled droplets often continued movement immediately after the trap was turned off, and multiple "pullbacks" were often seen (the droplet reached the edge of the trap, stalled, presumably detached from the MT, and was rapidly pulled back to the center of the trap), indicating continued activity of motors while inside the trap.

An arrested droplet might, in principle, continue to travel relative to the MT, causing it to buckle instead. This effect, however, seems negligible: fast-moving droplets that were first stalled, held for a few seconds, and then released showed no rebound reflecting straightening of a buckled MT.

Acknowledgments

M. A. W. thanks S. Kramer and Y. Ahmed for technical advice. S. P. G. is a recipient of NIH postdoctoral traineeship 5F32GM18329 from the NIGMS and acknowledges helpful discussions with M. Schnitzer and K. Visscher. M. P. was supported by a predoctoral traineeship from the NIGMS. S. M. B. and S. P. G. were supported by grant 5R01GM5143 from the NIGMS. E. F. W. and M. A. W. gratefully acknowledge support from the Howard Hughes Medical Institute and grant 5R37HD15587 from the NICHD. The authors thank J. Fischer-Vize and C. Nüsslein-Volhard for providing fly strains, and J. Fischer-Vize for generously sharing unpublished data on *marbles*.

Received November 14, 1997; revised January 9, 1998.

References

Ashkin, A., Schütze, K., Dziedzic, J.M., Euteneuer, U., and Schliwa, M. (1990). Force generation of organelle transport measured *in vivo* by an infrared laser trap. Nature *348*, 346–348.

Bereiter-Hahn, J., Fox, C.H., and Thorell, B. (1979). Quantitative reflection contrast microscopy of living cells. J. Cell Biol. *82*, 767–779.

Bevington, P.R. (1969). Data Reduction and Error Analysis for the Physical Sciences (New York: McGraw-Hill).

Brady, S.T., Lasek, R.J., and Allen, R.D. (1985). Video microscopy of fast axonal transport in extruded axoplasm: a new model for study of molecular mechanisms. Cell Motil. *5*, 81–101.

Edgar, B.A., Odell, G.M., and Schubiger, G. (1987). Cytoarchitecture and the patterning of *fushi tarazu* expression in the *Drosophila* blastoderm. Genes Dev. *1*, 1226–1237.

Fan, S.-S., and Ready, D.F. (1997). *Glued* participates in distinct microtubule-based activities in *Drosophila* eye development. Development *124*, 1497–1507.

Fischer-Vize, J.A., and Mosley, K.L. (1994). *Marbles* mutants: uncoupling cell determination and nuclear migration in the developing *Drosophila* eye. Development. *120*, 2609–2618.

Foe, V.E., and Alberts, B.M. (1983). Studies of nuclear and cytoplasmic behavior during the five mitotic cycles that precede gastrulation in *Drosophila* embryogenesis. J. Cell Sci. *61*, 31–70.

Fullilove, S.L., and Jacobson, A.G. (1971). Nuclear elongation and cytokinesis in *Drosophila montana*. Dev. Biol. *26*, 560–577.

Garcia-Alonso, L.A., and Garcia-Bellido, A. (1988). *Extramacrochaetae*, a trans-acting gene of the *achaete-scute* complex of *Drosophila* involved in cell communication. Roux's Arch. Dev. Biol. *197*, 328–338.

Gelles, J., Schnapp, B.J., and Sheetz, M.P. (1988). Tracking kinesin-driven movements with nanometer-scale precision. Nature *331*, 450–453.

Gepner, J., Li, M.-G., Ludmann, S., Kortas, C., Boylan, K., Iyadurai, S.J.P., McGrail, M., and Hays, T.S. (1996). Cytoplasmic dynein function is essential in *Drosophila melanogaster*. Genetics *142*, 865–878.

Giniger, E., Wells, W., Jan, L.Y., and Jan, Y.N. (1993). Tracing neurons with a kinesin β-galactosidase fusion protein. Roux's Arch. Dev. Biol. *202*, 112–122.

Grafstein, B., and Forman, D.S. (1980). Intracellular transport in neurons. Physiol. Rev. *60*, 1167–1283.

Greenspan, P., Mayer, E.P., and Fowler, S.D. (1985). Nile Red: a selective fluorescent stain for intracellular lipid droplets. J. Cell Biol. *100*, 965–973.

Hamm-Alvarez, S.F., Kim, P.Y., and Sheetz, M.P. (1993). Regulation of vesicle transport in CV-1 cells and extracts. J. Cell Sci. *106*, 955–966.

Hurd, D.D., and Saxton, W.M. (1996). Kinesin mutations cause motor neuron disease phenotypes by disrupting fast axonal transport in *Drosophila*. Genetics *144*, 1075–1085.

Hyman, A.A., and Mitchison, T.J. (1991). Two different microtubule-based motor activities with opposite polarities in kinetochores. Nature *351*, 206–211.

Lee, K.D., and Hollenbeck, P.J. (1995). Phosphorylation of kinesin *in vivo* correlates with organelle association and neurite outgrowth. J. Biol. Chem. *270*, 5600–5605.

Merrill, P.T., Sweeton, D., and Wieschaus, E. (1988). Requirements for autosomal gene activity during precellular stages of *Drosophila melanogaster*. Development *104*, 495–509.

Morris, N.R., Xiang, X., and Beckwith, S.M. (1995). Nuclear migration advances in fungi. Trends Cell Biol. *5*, 278–282.

Nüsslein-Volhard, C., Frohnhöfer, H.G., and Lehmann, R. (1987). Determination of anteroposterior polarity in *Drosophila*. Science *238*, 1675–1681.

Parsons, S.F., and Salmon, E.D. (1997). Microtubule assembly in clarified *Xenopus* egg extracts. Cell Motil. Cytoskeleton *36*, 1–11.

Preece, A. (1972). A Manual for Histologic Technicians, 3rd Edition (Boston: Little, Brown, and Company).

Ray, S., Meyhöfer, E., Milligan, R.A., and Howard, J. (1993). Kinesin follows the microtubule's protofilament axis. J. Cell Biol. *121*, 1083–1093.

Rickoll, W.L. (1976). Cytoplasmic continuity between embryonic cells and the primitive yolk sac during early gastrulation in *Drosophila melanogaster*. Dev. Biol. *49*, 304–310.

Sato-Yoshitake, R., Yorifuji, H., Inagaki, M., and Hirokawa, N. (1992). The phosphorylation of kinesin regulates its binding to synaptic vesicles. J. Biol. Chem. *267*, 23930–23936.

Saxton, W.M., Hicks, J., Goldstein, L.S.B., and Raff, E.C. (1991). Kinesin heavy chain is essential for viability and neuromuscular functions in *Drosophila*, but mutants show no defects in mitosis. Cell *64*, 1093–1102.

Schliwa, M., Shimizu, T., Vale, R.D., and Euteneuer, U. (1991). Nucleotide specificities of anterograde and retrograde organelle transport in *Reticulomyxa* are indistinguishable. J. Cell Biol. *112*, 1199–1203.

Svoboda, K., and Block, S.M. (1994a). Biological applications of optical forces. Annu. Rev. Biophys. Biomol. Struct. *23*, 247–285.

Svoboda, K., and Block, S.M. (1994b). Force and velocity measured for single kinesin molecules. Cell *77*, 773–784.

Svoboda, K., Schmidt, C.F., Schnapp, B.J., and Block, S.M. (1993). Direct observation of kinesin stepping by optical trapping interferometry. Nature *365*, 721–727.

Thaler, C.D., and Haimo, L.T. (1992). Control of organelle transport in melanophores: regulation of Ca^{2+} and cAMP levels. Cell Motil. Cytoskeleton *22*, 175–184.

Thaler, C.D., and Haimo, L.T. (1996). Microtubules and microtubule motors: mechanisms of regulation. Int. Rev. Cytol. *164*, 269–327.

Tiffany, J.M. (1986). Refractive index of meibomian and other lipids. Curr. Eye Res. *5*, 887–889.

Tomlinson, A. (1985). The cellular dynamics of pattern formation in the eye of *Drosophila*. J. Embryol. Exp. Morph. *89*, 313–331.

Vale, R.D., Malik, F., and Brown, D. (1992). Directional instability of microtubule transport in the presence of kinesin and dynein, two opposite polarity motor proteins. J. Cell Biol. *119*, 1589–1596.

Valkenburg, J.A.C., and Woldringh, C.L. (1984). Phase separation between nucleiod and cytoplasm in *Escherichia coli* as defined by immersive refractometry. J. Bacteriol. *160*, 1151–1157.

Visscher, K., Gross, S.P., and Block, S.M. (1996). Construction of multiple-beam optical traps with nanometer-resolution position sensing. IEEE Sel. Top. Quant. Elect. *2*, 1066–1076.

Wang, S., and Hazelrigg, T. (1994). Implications for *bcd* mRNA localization from spatial distribution of Exu protein in *Drosophila* oogenesis. Nature *369*, 400–403.

Wang, Z., Khan, S., and Sheetz, M.P. (1995). Single cytoplasmic dynein molecule movements: characterization and comparison with kinesin. Biophys. J. *69*, 2011–2023.

Weast, R. (1986). CRC Handbook of Chemistry and Physics, 67th Edition (Boca Raton, FL: CRC Press, Inc.), e374–e375.

White, G., Pencer, J., Nickel, B.G., Wood, J.M., and Hallett, F.R. (1996). Optical changes in unilamellar vesicles experiencing osmotic stress. Biophys. J. *71*, 2701–2715.

Wieschaus, E., and Nüsslein-Volhard, C. (1986). Looking at embryos. In *Drosophila*: A Practical Approach, D.B. Roberts, Ed. (Oxford: IRL Press), pp. 199–227.